SCIENCE CHINA
Earth Sciences

•RESEARCH PAPER•

June 2021 Vol.64 No.6: 992–1004
https://doi.org/10.1007/s11430-021-9784-7

An unsplit complex frequency-shifted perfectly matched layer for second-order acoustic wave equations

Xiuzheng FANG[1,2] & Fenglin NIU[1,2*]

[1] *State Key Laboratory of Petroleum Resources and Prospecting, and Unconventional Petroleum Research Institute, China University of Petroleum, Beijing 102249, China;*
[2] *Department of Earth, Environmental and Planetary Sciences, Rice University, Houston, Texas 77005, USA*

Received January 12, 2021; revised April 9, 2021; accepted May 7, 2021; published online May 18, 2021

Abstract The perfectly matched layer (PML) boundary condition has been proven to be effective for attenuating reflections from model boundaries during wavefield simulation. As such, it has been widely used in time-domain finite-difference wavefield simulations. The conventional PML has poor performance for near grazing incident waves and low-frequency reflections. To overcome these limitations, a more complex frequency-shifted stretch (CSF) function is introduced, which is known as the CFS-PML boundary condition and can be implemented in the time domain by a recursive convolution technique (CPML). When implementing the PML technique to second-order wave equations, all the existing methods involve adding auxiliary terms and rewriting the wave equations into new second-order partial differential equations that can be simulated by the finite-difference scheme, which may affect the efficiency of numerical simulation. In this paper, we propose a relatively simple and efficient approach to implement CPML for the second-order equation system, which solves the original wave equations numerically in the stretched coordinate. The spatial derivatives in the stretched coordinate are computed by adding a correction term to the regular derivatives. Once the first-order spatial derivatives are computed, we computed the second-order spatial derivatives in a similar way; therefore, we refer to the method as two-step CPML (TS-CPML). We apply the method to the second-order acoustic wave equation and a coupled second-order pseudo-acoustic TTI wave equation. Our simulations indicate that amplitudes of reflected waves are only about half of those computed with the traditional CPML method, suggesting that the proposed approach has computational advantages and therefore can be widely used for forwarding modeling and seismic imaging.

Keywords PML, CPML, Absorbing boundary condition, Finite-difference, Second-order wave equation, Numerical modeling

Citation: Fang X, Niu F. 2021. An unsplit complex frequency-shifted perfectly matched layer for second-order acoustic wave equations. Science China Earth Sciences, 64(6): 992–1004, https://doi.org/10.1007/s11430-021-9784-7

1. Introduction

Simulation of seismic wavefield propagation through complex media is a common approach to quantitatively study the Earth's interior. Due to its simplicity of implementation and high accuracy to solutions of partial differential equations, time-domain finite-difference (TDFD) methods become the most dominant approach for seismic wavefield simulation (Alford et al., 1974; Kelly et al., 1976; Marfurt, 1984; Virieux, 1984, 1986; Levander, 1988; Graves, 1996; Saenger et al., 2000; Liu and Sen, 2009; Wang et al., 2014). In general, finite-difference (FD) simulations are performed within a finite model space. As such, a proper absorbing boundary condition is required to attenuate undesired reflections from the artificial boundaries of a truncated modeling domain. Numerous approaches have been developed aiming for such an ideal absorbing boundary condition with various efficiency and stability. Among them, the perfectly matched layers (PML) method, first proposed by Bérenger (1994) for electromagnetic wave simulation, has proven to be the most

* Corresponding author (email: niu@rice.edu)

robust and efficient absorbing boundary condition for FD simulation in a truncated domain.

In theory, the PML method causes no reflection at the interface between the perfectly matched layer and the interior of the model in a continuous domain for all angles of incidence and frequency. It has become a widely adopted absorbing boundary method in seismic modeling and imaging for both acoustic and elastic waves in isotropic and anisotropic media (Chew and Liu, 1996; Hastings et al., 1996; Collino and Tsogka, 2001; Marcinkovich and Olsen, 2003; Festa and Nielsen, 2003; Wang and Tang, 2003; Basu and Chopra, 2004; Kreiss and Duru, 2013; Li et al., 2018; Ma et al., 2018, 2019a, 2019b). However, due to numerical discretization, the effectiveness of the conventional PML method degrades for waves with grazing incidences at low frequency (Festa and Vilotte, 2005; Komatitsch and Martin, 2007; Drossaert and Giannopoulos, 2007a, 2007b). By extending the concept of coordinate stretching from the convention PML approach, Kuzuoglu and Mittra (1996) first proposed a complex frequency-shifted PML (CFS-PML) for electromagnetic wave simulation. Many studies extended this approach to seismic wave simulation and showed that the proposed CFS-PML approach yields better absorbing performance in the previously mentioned challenging cases when compared with the conventional PML approach (Bérenger, 2002a, 2002b; Becache et al., 2004; Festa et al., 2005; Festa and Vilotte, 2005; Drossaert and Giannopoulos, 2007a, 2007b; Komatitsch and Martin, 2007; Martin et al., 2008; Martin and Komatitsch, 2009).

In order to effectively implement CFS-PML, Roden and Gedney (2000) introduced a recursive convolution technique (referred to as CPML) to solve the unsplit wavefield in electromagnetic modeling. The same approach has been applied to the first-order partial differential equations of elastic wavefield (e.g., Drossaert and Giannopoulos, 2007a, 2007b; Komatitsch and Martin, 2007), viscoelastic and poroelastic wavefields (Martin et al., 2008; Martin and Komatitsch, 2009), and other wavefields (Chen et al., 2014). Alternatively, one can introduce auxiliary differential equations, which can be incorporated into the PML/CPML formulations to avoid the convolution operation (Ramadan, 2003; Martin et al., 2010; Zhang and Shen, 2010; Zhang et al., 2014).

For a second-order equation system, there are two different ways of implementing the unsplit-field PML/CPML. The first category is to transform the second-order equation system to the first-order equation system, which can be solved efficiently by introducing auxiliary differential equations (Martin et al., 2010; Zhang and Shen, 2010) or by the CPML method. This approach belongs to the PML implementation of the first-order differential equations. The second approach aims to transform the original wave equation into a new second-order differential equation that can be simulated with FD. This type of PML implementation needs to add either auxiliary differential equations to the second-order acoustic CPML equation (Appelö and Kreiss, 2007; Gao et al., 2015) and elastic CPML equation (Li and Matar, 2010; Duru and Kreiss, 2012; Ma et al., 2019b) or auxiliary parameters to the second-order equations, such as the revised second-order acoustic wave equation (Pasalic and McGarry, 2010) and the revised elastic wave equation (Ma et al., 2018, 2019a). This second approach increases either the number of equations or the number of unknown parameters in the equations, which complicates the PML implementation of the second-order equation.

In this paper, we propose a new implementation of unsplit CPML for the second-order acoustic wave equation system without transforming the wave equation and introducing new parameters. Basically, we compute the spatial derivatives in the stretched coordinate directly by adding a correction term to the regular spatial derivative. For a second-order differential equation, we simply apply the first-order spatial derivatives twice in the same way. Hence, we refer to this two-step CPML as TS-CPML.

The rest of this paper is structured as follows: we will first give a brief review of the PML and CPML methods. We then present a detailed description of the TS-CPML implementation. Finally, we present several numerical simulations using isotropic and tilted transverse isotropic (TTI) media to demonstrate the performance of the TS-CPML method.

2. The PML theory and its implementations

2.1 PML method

First, let us briefly review the theory of the PML method. We set up PML in the vertical strip $a<x<b$ (see Figure 1a). We refer to the area of $x<a$ as the computational domain and area of $a<x<b$ area as the PML domain. The basic principle of the PML model is to couple the equation in the computational domain with an equation in the PML domain such that there is no reflection at the interface $x=a$, and that the wave's energy decreases exponentially in the PML domain. Let us consider a two-dimensional acoustic plane wave $u(\theta, \omega)$ that arrives from $x<a$ at an incident angle of θ with respect to the x axis. The differential form of the linear acoustic wave in the frequency domain can be written as:

$$\nabla^2 \hat{u} + k^2 \hat{u} = 0, \tag{1}$$

where $\hat{u}$ is the pressure wavefield in the frequency domain, $k=\omega/v$ is the wave number, with ω being the angular frequency and v the velocity (or wave speed). Moreover, $k_x = k\cos\theta$ and $k_z = k\sin\theta$, with θ being the incidence angle at the interface (Figure 1a). The harmonic solution of eq. (1) is the plane wave:

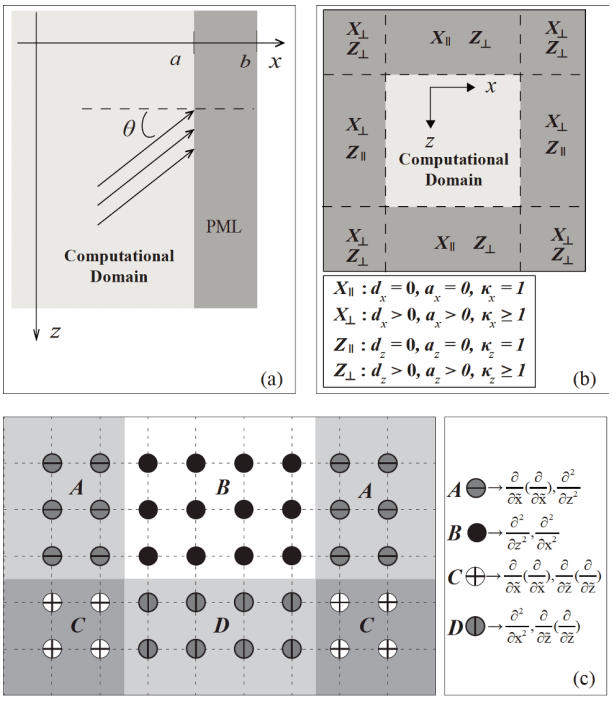

Figure 1 (a) Schematic diagram showing a plane wave propagating from the computational domain to the PML layer. (b) A 2-D rectangular computational domain (light grey) surrounding by PML layers (dark grey) and the PML parameters setting diagram. (c) Finite-difference scheme of the second-order spatial derivative in computational domain A and PML domain B, C, and D.

$$\hat{u} = \mathrm{e}^{-\mathrm{j}(k_x x + k_z z)}, \tag{2}$$

where j denotes imaginary unit. The main idea of the PML technique is that the waves generated in the computational domain (interior zone) can travel to the PML zone without reflection at the interface (x=a) and their energy decays in the PML domain. Following Collino and Tsogka (2001), a new complex coordinate $\tilde{x}$ is introduced in the PML domain:

$$\begin{cases} \dfrac{\partial \tilde{x}}{\partial x} = \hat{s}_x = 1 + \dfrac{d_x}{\mathrm{j}\omega}, \\ \tilde{x} = x - \dfrac{\mathrm{j}}{\omega}\displaystyle\int_0^x d_x \,\mathrm{d}x, \end{cases} \tag{3}$$

where d_x is an absorbing function in the PML domain and the subscript x is the label for the x axis. Eq. (3) also means that in the frequency domain the partial derivative in the stretched coordinate is scaled to the regular partial derivative by a factor of $1/\hat{s}_x$:

$$\frac{\partial}{\partial \tilde{x}} = \frac{1}{\hat{s}_x}\frac{\partial}{\partial x}. \tag{4}$$

We can see that the PML model involves a simple substitution and can be viewed as an analytical continuation of the real coordinates in the complex space. Readers are referred to Collino and Tsogka (2001) and Komatitsch and Martin (2007) for more details. Substituting eq. (3) into eq. (2), we can get the plane wave solution in the PML domain as:

$$\begin{aligned} \hat{u}_{\mathrm{pml}} &= (\mathrm{e}^{-\mathrm{j}k_x \tilde{x}})\mathrm{e}^{-\mathrm{j}k_z z} \\ &= \left(\mathrm{e}^{-\mathrm{j}k_x x}\mathrm{e}^{-\frac{k_x}{\omega}\int_0^x d_x \,\mathrm{d}x}\right)\mathrm{e}^{-\mathrm{j}k_z z} \\ &= \hat{u}\mathrm{e}^{-\frac{k_x}{\omega}\int_0^x d_x \,\mathrm{d}x}, a < x < b. \end{aligned} \tag{5}$$

Eq. (5) implies that the wave decays by a factor of $\exp\left\{-\dfrac{k_x}{\omega}\displaystyle\int_0^x d_x \,\mathrm{d}x\right\}$ in the PML zone. Due to k_x=$k$cosθ, a wave propagating closes to the normal incidence generally has better absorbing performance in the PML zone. It also implies that the classical PML method is less efficient in the case of very thin mesh slices with a wave propagating at grazing incidence as k_x is close zero when the incident angle θ approaches to 90°.

2.2 The CPML technique

The key difference between the classical PML and the CFS-PML is the stretching function $\hat{s}_x$. The classical PML stretching function is defined as $\hat{s}_x = 1 + \dfrac{d_x}{\mathrm{j}\omega}$, while the CFS-PML stretching function $\hat{s}_x$ can be written as:

$$\hat{s}_x = \kappa_x + \frac{d_x}{a_x + \mathrm{j}\omega}, \tag{6}$$

where $a_x \geq 0$ is the frequency-shifted factor and $\kappa_x \geq 1$ is the scaling factor. Obviously, if we set κ_x=1 and a_x=0, we obtain the regular PML stretching function. d_x is a damping function that attenuates the wavefield exponentially inside the PML region. In this study, we set κ_x=1, κ_z=1. Assuming that the computational domain is a 2D rectangular area as shown in Figure 1b, we set d_x>0, κ_x=1, a_x>0 and d_z=0, κ_z=1, a_z=0 in the PML region with x axis normal towards the interface to make sure that the wavefield components propagating in the x direction are absorbed in PML domain. Accordingly, we can set d_z>0, κ_z=1, a_z>0 and d_x=0, κ_x=1, a_x=0 in the PML region with z axis normal towards the interface to absorb the wavefield components propagating in the z direction.

In the time-domain, the partial derivative in the stretched coordinate is shown in eq. (4) can be written as a convolution of the inverse Fourier transform of the stretch function $1/\hat{s}_x$, and the regular partial derivative:

$$\frac{\partial}{\partial \tilde{x}} = F^{-1}\left\{\frac{1}{\hat{s}_x}\right\} * \frac{\partial}{\partial x} = \frac{1}{s_x} * \frac{\partial}{\partial x}, \tag{7}$$

where F^{-1} denotes the inverse Fourier transform. This approach, which employs a convolution to link the partial derivative between the stretched and regular coordinates, is usually referred to as CPML, which turned out to be an efficient implementation of CFS-PML.

It can be shown that the partial derivative in the stretched coordinate can be further written as (e.g., Komatitsch and

Martin, 2007; Pasalic and McGarry, 2010):

$$\begin{cases} \dfrac{\partial}{\partial \tilde{x}} = \dfrac{1}{\kappa_x}\dfrac{\partial}{\partial x} + \psi_x^t, \\ \psi_x^t = \zeta_x(t) * \dfrac{\partial}{\partial x}, \\ \zeta_x(t) = -\dfrac{d_x}{\kappa_x^2} H(t) \mathrm{e}^{-\left(\frac{d_x}{\kappa_x}+a_x\right)t}, \end{cases} \tag{8}$$

where $H(t)$ is the Heaviside function and ψ_x^t is known as the time convolution term, which is an operator instead of a function. This operator can be represented in a recursive format. In particular, the discrete-time function $\psi_x^{n\Delta t}$ can be explicitly written as:

$$\begin{cases} \psi_x^{n\Delta t} = b_x \psi_x^{(n-1)\Delta t} + c_x \dfrac{\partial^{n\Delta t}}{\partial x}, \\ b_x = \mathrm{e}^{-\left(\frac{d_x}{\kappa_x}+a_x\right)\Delta t}, \\ c_x = \dfrac{d_x}{d_x\kappa_x + a_x\kappa_x^2}(b_x - 1), \end{cases} \tag{9}$$

where n denotes the nth time step. Therefore, the convolution term at each time step, $\psi_x^{n\Delta t}$, can be obtained by their values at the previous time step and the spatial derivatives at the present time step.

2.3 TS-CPML for the second-order wave equation

The original second-order acoustic wave PML/CPML equation is:

$$\begin{aligned} \frac{1}{v^2}\frac{\partial^2 u}{\partial t^2} &= \frac{\partial}{\partial \tilde{x}}\left(\frac{\partial u}{\partial \tilde{x}}\right) + \frac{\partial}{\partial \tilde{z}}\left(\frac{\partial u}{\partial \tilde{z}}\right) \\ &= \frac{1}{s_x} * \frac{\partial}{\partial x}\left(\frac{1}{s_x} * \frac{\partial u}{\partial x}\right) + \frac{1}{s_z} * \frac{\partial}{\partial z}\left(\frac{1}{s_z} * \frac{\partial u}{\partial z}\right), \end{aligned} \tag{10}$$

where u is the wavefield and v is the velocity (or wave speed). Because of the two-fold convolution operation, it is difficult to discretize eq. (10) directly using a finite difference scheme in time domain. As mentioned above, all the previous studies introduced additional parameters to transform eq. (10) into a new second-order partial differential equation without the convolution operation. Instead of re-writing the original CPML eq. (10), we propose to directly compute spatial derivative by two-step strategy using eqs. (8) and (9):

$$\frac{\partial u^{n\Delta t}}{\partial \tilde{x}} = \frac{\partial u^{n\Delta t}}{\partial x} + \psi_x^{n\Delta t}(u^{n\Delta t}). \tag{11}$$

Here we set κ_x=1. Eq. (11) means that at each time step the partial derivative in the stretched coordinate can be computed by adding the convolution term to the regular partial derivative, i.e., we can consider the convolution term as a correction term and use eq. (9) to compute it at each time step.

To further elaborate our FD scheme, we first introduce two FD operators, D_x^+ and D_x^-, which represent the forward and backward finite-difference operator in the x direction:

$$\begin{cases} D_x^+ u(i,k) = \sum_{m=1}^{M} c_m [u(i\Delta x + m\Delta x, k\Delta z) \\ \qquad -u(i\Delta x - (m-1)\Delta x, k\Delta z)] / \Delta x, \\ D_x^- u(i,k) = \sum_{m=1}^{M} c_m [u(i\Delta x + (m-1)\Delta x, k\Delta z) \\ \qquad -u(i\Delta x - m\Delta x, k\Delta z)] / \Delta x, \end{cases} \tag{12}$$

where and in the upcoming section i and k are discretization indices along the x-axis and z-axis, respectively. Δx and Δz are the grid size in the x-axis and z-axis. c_m, m=1,2,3..., are stagger-grid finite difference coefficients (Kindelan et al., 1990; Liu, 2014). For example, in the case of fourth order in space, M=2, the finite-difference coefficients c_1=9/8 and c_2=-1/24.

When implementing eq. (11) in computing the first-order derivatives, we first employed the forward FD operator to compute the regular partial derivative at half-grid point:

$$\left.\frac{\partial u^{n\Delta t}}{\partial x}\right|_{(i\Delta x+1/2\Delta x, k\Delta z)} = D_x^+ u^n(i,k) = u_x^n(i+1/2,k), \tag{13}$$

where u_x represents the first order spatial derivative of the wavefield, u. Then we added the convolution term to the regular partial derivative to obtain the spatial derivative in the stretched coordinate:

$$\begin{aligned} \left.\frac{\partial u^{n\Delta t}}{\partial \tilde{x}}\right|_{(i\Delta x+1/2\Delta x, k\Delta z)} &= u_{\tilde{x}}^n(i+1/2,k) \\ &= u_x^n(i+1/2,k) + b_x(i+1/2,k) \\ &\quad \cdot \psi_x^{n-1}(u_x^{n-1}(i+1/2,k)) \\ &\quad + c_x(i+1/2,k) u_x^n(i+1/2,k). \end{aligned} \tag{14}$$

Once the first partial derivatives of the wavefield, $u_{\tilde{x}}^n(i+1/2,k)$, were computed, we employed the similar scheme to compute the second-order derivative of the wavefield in the stretched coordinate:

$$\begin{cases} \left.\dfrac{\partial u_{\tilde{x}}^n}{\partial x}\right|_{(i\Delta x, k\Delta z)} = D_x^- u_{\tilde{x}}^n(i+1/2,k) \\ = \sum_{m=1}^{M} \dfrac{c_m[u_{\tilde{x}}^n(i-1/2+m,k) - u_{\tilde{x}}^n(i+1/2-m,k)]}{\Delta x} \\ = u_{x\tilde{x}}^n(i,k), \\ \left.\dfrac{\partial u_{\tilde{x}}^n}{\partial \tilde{x}}\right|_{(i\Delta x, k\Delta z)} = u_{\tilde{x}\tilde{x}}^n(i,k) \\ = u_{x\tilde{x}}^n(i,k) + b_x(i,k)\psi_x^{n-1}(u_{x\tilde{x}}^{n-1}(i,k)) \\ \quad + c_x(i,k) u_{x\tilde{x}}^n(i,k). \end{cases} \tag{15}$$

Here we employed the backward FD operator in computing the regular spatial derivatives. It should be noted that our scheme is applicable for any high-order FD stencils.

For a 2D rectangular area with a free surface (Figure 1c),

we simply took away the top PML layer in Figure 1b and applied the finite difference directly to the second-order spatial derivatives in the computational and PML domains:

$$\begin{cases} \dfrac{\partial^2 u}{\partial x^2} = \dfrac{1}{\Delta x^2}\left(C_0 u(i,k) + \sum\limits_{l=1}^{L} C_l(u(i+l,k) + u(i-l,k))\right), \\ \dfrac{\partial^2 u}{\partial z^2} = \dfrac{1}{\Delta z^2}\left(C_0 u(i,k) + \sum\limits_{l=1}^{L} C_l(u(i,k+l) + u(i,k-l))\right), \end{cases} \tag{16a}$$

$$\begin{cases} \dfrac{\partial}{\partial \tilde{x}}\left(\dfrac{\partial u}{\partial \tilde{x}}\right) = D_{\tilde{x}}^{-} D_{\tilde{x}}^{+} u(i,k), \\ \dfrac{\partial}{\partial \tilde{z}}\left(\dfrac{\partial u}{\partial \tilde{z}}\right) = D_{\tilde{z}}^{-} D_{\tilde{z}}^{+} u(i,k), \end{cases} \tag{16b}$$

Here C_l is coefficients of the $2L$-order central finite difference in the computational domain. $D_{\tilde{x}}^{-} D_{\tilde{x}}^{+} u(i,k)$ and $D_{\tilde{z}}^{-} D_{\tilde{z}}^{+} u(i,k)$ are the discretized scheme of $u_{\tilde{x}\tilde{x}}(i\Delta x, k\Delta z)$ and $u_{\tilde{z}\tilde{z}}(i\Delta x, k\Delta z)$, respectively. Thus, the discretized acoustic wave equation with $2L$-order finite-difference scheme in computational domain B became:

$$\begin{aligned} u^{n+1}(i,k) &= 2u^n(i,k) - u^{n-1}(i,k) \\ &+ \frac{v^2\Delta t^2}{\Delta x^2}\left(C_0 u^n(i,k) + \sum_{l=1}^{L} C_l(u^n(i+l,k) + u^n(i-l,k))\right) \\ &+ \frac{v^2\Delta t^2}{\Delta z^2}\left(C_0 u^n(i,k) + \sum_{l=1}^{L} C_l(u^n(i,k+l) + u^n(i,k-l))\right). \end{aligned} \tag{17}$$

In the PML domain A or D, the corresponding finite difference scheme are:

$$\begin{aligned} u^{n+1}(i,k) &= 2u^n(i,k) - u^{n-1}(i,k) + v^2\Delta t^2 D_{\tilde{x}}^{-} D_{\tilde{x}}^{+} u^n(i,k) \\ &+ \frac{v^2\Delta t^2}{\Delta z^2}\left(C_0 u^n(i,k) + \sum_{l=1}^{L} C_l(u^n(i,k+l) + u^n(i,k-l))\right), \end{aligned} \tag{18a}$$

$$\begin{aligned} u^{n+1}(i,k) &= 2u^n(i,k) - u^{n-1}(i,k) + v^2\Delta t^2 D_{\tilde{z}}^{-} D_{\tilde{z}}^{+} u^n(i,k) \\ &+ \frac{v^2\Delta t^2}{\Delta x^2}\left(C_0 u^n(i,k) + \sum_{l=1}^{L} C_l(u^n(i+l,k) + u^n(i-l,k))\right). \end{aligned} \tag{18b}$$

In the corner areas C (Figure 1c), the finite difference scheme can be expressed as:

$$\begin{aligned} u^{n+1}(i,k) &= 2u^n(i,k) - u^{n-1}(i,k) \\ &+ v^2\Delta t^2\left(D_{\tilde{x}}^{-} D_{\tilde{x}}^{+} u^n(i,k) + D_{\tilde{z}}^{-} D_{\tilde{z}}^{+} u^n(i,k)\right). \end{aligned} \tag{19}$$

Compared with the traditional CPML implementation of the second-order acoustic equation (Appendix A, https://link.springer.com), TS-CPML involves fewer parameters, and more importantly, avoids the calculation of the partial derivative of the convolution terms (Table 1).

2.4 TS-CPML for the pseudo-acoustic TTI wave equation

Following Fletcher et al. (2009), we employed a coupled second-order pseudo-acoustic wave equation for tilted transverse isotropic (TTI) media:

$$\begin{cases} \dfrac{\partial^2 p}{\partial^2 t} = v_{px}^2 H_2 p + \alpha v_{pz}^2 H_1 q + v_{sz}^2 H_1(p - \alpha q), \\ \dfrac{\partial^2 q}{\partial^2 t} = \dfrac{v_{pn}^2}{\alpha} H_2 p + v_{pz}^2 H_1 q - v_{sz}^2 H_2\left(\dfrac{1}{\alpha} p - \alpha q\right), \end{cases} \tag{20}$$

where,

$$\begin{cases} H_1 = \sin^2\theta \dfrac{\partial^2}{\partial \tilde{x}^2} + \cos^2\theta \dfrac{\partial^2}{\partial \tilde{z}^2} + \sin 2\theta \dfrac{\partial^2}{\partial \tilde{x}\,\partial \tilde{z}}, \\ H_2 = \dfrac{\partial^2}{\partial \tilde{x}^2} + \dfrac{\partial^2}{\partial \tilde{z}^2} - H_1. \end{cases} \tag{21}$$

Here p and q are the pressure wavefield and an auxiliary wavefield, respectively. v_{pz} and v_{sz} are the P and the SV velocity in the direction normal to the symmetry plane, respectively. $v_{pn} = v_{pz}\sqrt{1+2\delta}$ is the P-wave normal moveout (NMO) velocity, $v_{px} = v_{pz}\sqrt{1+2\varepsilon}$ is the P-wave velocity in the symmetry plane. δ and ε are the Thomsen anisotropic parameters (Thomsen, 1986). a is a nonzero scalar, and θ is the dip angle of the symmetry axis measured from vertical direction.

It is pretty straightforward to implement the TS-CPML scheme to compute the second-order spatial derivatives in eq. (21). Although there is a mixed second-order spatial derivative in eq. (21), it is also quite obvious to compute it numerically using the TS-CPML technique, i.e., first computing $p_{\tilde{z}}\left(i\Delta x, k\Delta z + \dfrac{\Delta z}{2}\right)$ and then $\dfrac{\partial^2 p}{\partial \tilde{x}\,\partial \tilde{z}}$ similar to eqs. (13)–(15). Note that the first-order spatial derivatives were computed at half grids and were further interpolated to the full grids:

Table 1 Comparison of TS-CPML and CPML in computing convolution terms and their first-order spatial derivatives in anisotropic media

Method	Convolution terms	First-order spatial derivatives
TS-CPML	$\psi_x(u), \psi_z(u), \psi_{\tilde{x}}\left(\dfrac{\partial u}{\partial \tilde{x}}\right), \psi_{\tilde{z}}\left(\dfrac{\partial u}{\partial \tilde{z}}\right)$	None
Traditional CPML	$\psi_x(u), \psi_z(u), \psi_x\left(\dfrac{\partial u}{\partial x}\right), \psi_z\left(\dfrac{\partial u}{\partial z}\right), \psi_x\left(\psi_x(u)\right), \psi_z\left(\psi_z(u)\right)$	$\dfrac{\partial}{\partial x}\psi_x(u), \dfrac{\partial}{\partial z}\psi_z(u)$

$$p_{\bar{z}}(i\Delta x, k\Delta z) = \frac{1}{2}\left(p_{\bar{z}}\left(i\Delta x, k\Delta z + \frac{\Delta z}{2}\right) + p_{\bar{z}}\left(i\Delta x, k\Delta z - \frac{\Delta z}{2}\right)\right). \quad (22)$$

Similarly, the second-order derivatives were computed in the half grids in the x direction, and then averaged to the whole grids:

$$p_{\bar{x}\bar{z}}(i\Delta x, k\Delta z) = \frac{1}{2}\left(p_{\bar{x}\bar{z}}(i\Delta x + \frac{\Delta x}{2}, k\Delta z) + p_{\bar{x}\bar{z}}(i\Delta x - \frac{\Delta x}{2}, k\Delta z)\right). \quad (23)$$

Table 2 shows the comparison of computing terms required in solving the second-order pseudo-acoustic wave equation in a tilted transverse isotropic (TTI) medium between the traditional CPML implementation method (Appendix B) and TS-CPML method.

3. Numerical test

As we have shown in the previous sections, TS-CPML can be directly used to solve the second-order wave equations in isotropic and TTI anisotropic media. To verify its accuracy and absorbing performance, we have conducted extensive numerical tests with various types of 2-D acoustic velocity models. In all the following 2-D numerical examples, we employed a finite-difference scheme that is second order in time and sixth order in space in computational and PML domain. If not specified, the finite difference grid is uniform with a grid spacing $\Delta x = \Delta z = 50$ m and the time step is $\Delta t = 5$ ms.

3.1 Homogeneous model

In our first test, we chose a homogeneous isotropic velocity model (Figure 2a) with a wave speed 3000 m s^{-1}. We set the model size to be 10 km×10 km and employed an explosive Ricker wavelet source with a dominant frequency 5 Hz, which was placed at the center of the model. To satisfy the null initial condition, we shifted the Ricker wavelet function by t_0=1.5/f_0=0.3s in time. We kept the duration of simulation to 10 s, which comprises 2000 timesteps.

Following Martin and Komatitsch (2009), we employed the following equations for the three parameters in the CPML stretching function:

Table 2 Comparison of TS-CPML and CPML in computing convolution terms and their first-order spatial derivatives in a TTI medium

Method	Convolution terms	First-order spatial derivatives
TS-CPML	$\psi_x(p), \psi_z(p), \psi_x\left(\frac{\partial p}{\partial \bar{x}}\right), \psi_z\left(\frac{\partial p}{\partial \bar{z}}\right), \psi_x\left(\frac{\partial p}{\partial \bar{z}}\right),$ $\psi_x(q), \psi_z(q), \psi_x\left(\frac{\partial q}{\partial \bar{x}}\right), \psi_z\left(\frac{\partial q}{\partial \bar{z}}\right), \psi_x\left(\frac{\partial q}{\partial \bar{z}}\right)$	None
Traditional CPML	$\psi_x(p), \psi_z(p), \psi_x\left(\frac{\partial p}{\partial x}\right), \psi_z\left(\frac{\partial p}{\partial z}\right), \psi_x\left(\frac{\partial p}{\partial z}\right),$ $\psi_x(q), \psi_z(q), \psi_x\left(\frac{\partial q}{\partial x}\right), \psi_z\left(\frac{\partial q}{\partial z}\right), \psi_x\left(\frac{\partial q}{\partial z}\right),$ $\psi_x\left(\psi_x(p)\right), \psi_z\left(\psi_z(p)\right),$ $\psi_x\left(\psi_x(q)\right), \psi_z\left(\psi_z(q)\right)$	$\frac{\partial}{\partial x}\left(\psi_x(p)\right), \frac{\partial}{\partial z}\left(\psi_z(p)\right),$ $\frac{\partial}{\partial x}\left(\psi_x(q)\right), \frac{\partial}{\partial z}\left(\psi_z(q)\right),$ $\frac{\partial}{\partial x}\left(\psi_z(p)\right), \frac{\partial}{\partial x}\left(\psi_z(q)\right)$

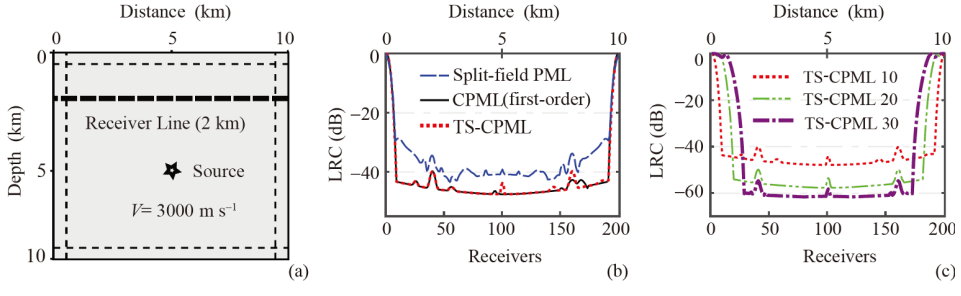

Figure 2 Model and results of LRCs. (a) The 2-D homogeneous model is 10 km×10 km in dimension and has an acoustic velocity of 3000 m s^{-1}. The thin dashed lines represent the boundaries between the computational and PML domains. The thick horizontal dashed line indicates the locations (2 km in depth) of the 201 receivers, from which the local reflection coefficients (LRCs) are measured and shown in (b) and (c). (b) LRCs measured at the 201 receivers from simulation B (split-field PML), simulation C (CPML, first-order) and simulation D (TS-CPML) are shown in blue dashed, black solid and red dotted lines, respectively. Note a 10-cell thick PML layer is used in all the simulations. (c) LRCs measured at the 201 receivers from the TS-CPML synthetics computed with a 10-cell thick, 20-cell thick, and 30-cell thick PML layer are shown in red dotted, green and brown dash-dotted lines, respectively.

$$\begin{cases} d_{x_i} = d_0\left(x_i / L\right)^m, x_i = x, z; \\ \kappa_{x_i} = 1 + \left(\kappa_0 - 1\right)\left(x_i / L\right)^2, x_i = x, z; \\ a_{x_i} = a_0\left(1 - x_i / L\right), x_i = x, z, \end{cases} \tag{24}$$

where d_{x_i} is the absorbing function in the PML domain and x_i indicates the distance from the interior-PML interface into the PML zone along the x_i axis. L is the thickness of the PML and m=2. Following Collino and Tsogka (2001), the reference value for d_0 in the damping function was set to $d_0 = 3v_p \log\left((1+R_c)/(2L)\right)$ where R_c is the theoretical reflection coefficient and v_p is the acoustic wave velocity. We set κ_0=1 (Komatitsch and Martin, 2007), a_0=2πf_0 where f_0 is the dominant frequency of the Ricker wavelet.

To compare the amplitude of the reflected wave and its relative errors of different simulations, we first used a regular FD to compute a reference wavefield, $u_{ref}^{n\Delta t}(i\Delta x, k\Delta z)$, which can be considered as the accurate solution for a given source and velocity model. The velocity model needs to be large enough to avoid reflections from its boundaries to arrive before 10 s. In our simulation, we employed a (800Δx×800Δz) model, which is three times larger than the regular (200Δx×200Δz) models, to compute the reference solution. For each simulation with the TS-CPML and other existing PML/CPML techniques, we define the local reflection coefficient LRC(i,k):

$$\mathrm{LRC}(i,k) = \max\left(20\log_{10}\left(\frac{\left|u_{ref}^{n\Delta t}(i\Delta x, k\Delta z) - u_{sim}^{n\Delta t}(i\Delta x, k\Delta z)\right|}{\max\left|u_{ref}^{n\Delta t}(i\Delta x, k\Delta z)\right|}\right)\right), \tag{25}$$

Here $u_{ref}^{n\Delta t}(i\Delta x, k\Delta z)$ and $u_{sim}^{n\Delta t}(i\Delta x, k\Delta z)$ are the reference and simulated wavefield in the regular (200Δx×200Δz) model, respectively. For a specific grid point, the value of LRC(i,k) shows the absorbing performance of various PML/CPML implementations. The smaller the value is, the better the absorption performance at the point (i,k) is achieved.

For the sake of brevity in this paper, we hereafter referred to the reflecting boundary with conventional-grid finite-difference based on the second-order scalar wave equation as simulation A, the classical split-field PML boundary condition with stagger-grid finite-difference based on the first-order scalar wave equation as simulation B, the CPML boundary condition with stagger-grid finite-difference based on the first-order scalar wave equation as simulation C, and the proposed TS-CPML method for the second-order scalar wave equation as simulation D. In the simulations, B, C, and D, the PML/CPML thickness is set to 10 cells. In order to quantify the absorbing performance of simulation B, C and D, we computed LRC along a horizontal line at the depth of 40Δz, which is shown as the thick black dashed line in Figure 2a. Figure 2b shows the calculated LRCs of the three simulations, B, C and D using a 10-cell thick PML layer. The split-field PML (blue dashed line in Figure 2b) shows poorer absorbing performance than the two CPML methods (black solid line and red dotted line in Figure 2b), which have roughly the same performance. Figure 2c shows the comparison of the LRCs along the same horizontal receiver line in simulation D with a 10-cell thick, a 20-cell thick, and a 30-cell thick PML layer, respectively. From Figure 2c, we can see that as expected, increasing the PML layer thickness reduces the amplitude of the reflected waves and improves the absorption performance. More specifically, the LRCs of the 30-cell thick PML layer (about 2.5 times the dominant wavelength) is approximately equal to −60 dB, which means that the amplitude of the reflected waves from model boundaries is only about 0.1% of reflected waves without any absorbing.

Figure 3a shows wavefield snapshots of the simulations A, B, C, and D (from the top row to the bottom row) at four different times (1.5, 2.0, 2.5, and 3.0 s). The regular FD simulation A shows strong reflections from the model boundaries (top row of Figure 3a). We set a hypothetic receiver at the location (50Δx, 50Δz) (black reverse triangle in Figure 3a) to record seismogram in these simulations to quantify the relative errors. Figure 3b shows the synthetic seismograms at the receiver location calculated based on simulations B (blue dashed line), C (green dot-dashed line), and D (red dotted line). For comparison, we also show the reference synthetic seismogram at the same location in the black solid line. We can see that the reflection amplitude from the split-field PML boundary condition in simulation B is much larger than that of the CPML boundary condition in simulation C and the TS-CPML boundary condition in simulation D. On the other hand, amplitudes of the reflections from the TS-CPML and the CPML are roughly the same. Figure 3c shows the differences between the three TS-CPML synthetics (10-cell, 20-cell, and 30-cell thick PML layer) and the reference seismogram at the same hypothetic receiver. Increasing the CPML layer thickness could reduce the errors as shown in Figure 2c. From Figure 2c, we can see that a 10-cell thick PML can reduce artificial reflection to ~1% level, which is a precision for general wavefield simulations. However, if one wants to achieve a precision with errors <~0.1%, then a 30-cell thick PML layer (about 2.5 times the dominant wavelength) is required for this particular example.

To compare the absorbing and computational efficiency between the conventional CPML and the TS-CPML proposed here, we performed numerical simulations with the two implementations using a 2-D velocity model that has the same model parameters of the homogeneous model shown in Figure 2a except for a free surface on top (Figure 4a). The conventional CPML simulation is based on the method of

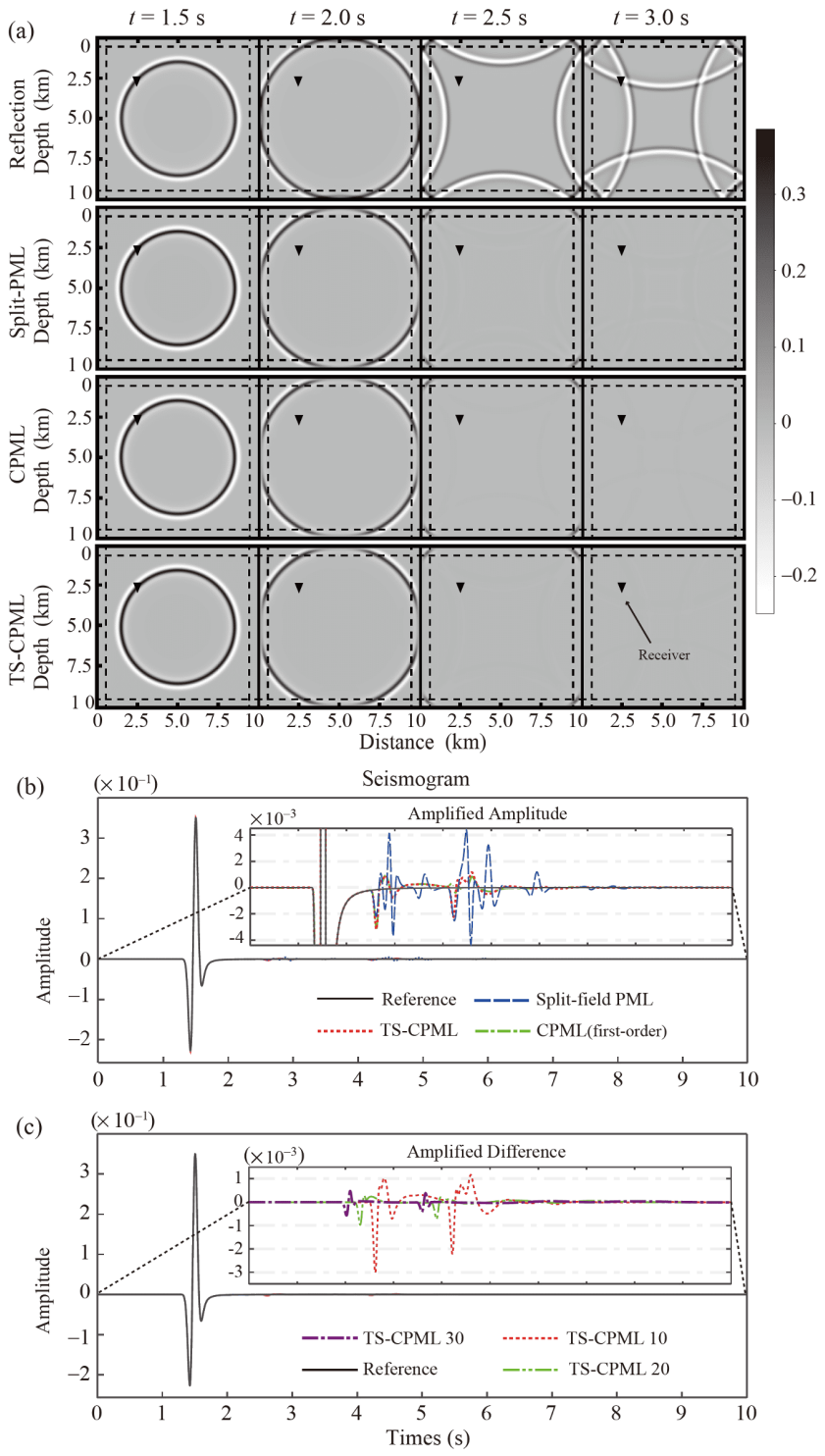

Figure 3 (a) Snapshots of the wavefield at 1.5, 2.0, 2.5 and 3.0 s with boundary conditions of reflection, split-field PML, CPML and TS-CPML, respectively, are shown from the top to the bottom. The thin dashed lines represent the boundaries between the computational and PML domains. The inverted solid triangle indicates the location of the recordings and results shown in (b) and (c). (b) Synthetic seismograms at (2.5 km, 2.5 km) (inverted solid triangle in (a)) computed with split-field PML, CPML and TS-CPML are shown in blue dashed, green dot-dashed and red dotted lines, respectively. For comparison, the reference seismogram is also shown in a black solid line. Inset shows the enlarged seismograms. (c) TS-CPML synthetics at (2.5 km, 2.5 km) (inverted solid triangle in (a)) computed with a 10-cell thick, 20-cell thick, and 30-cell thick PML layer are shown in red dotted, green and brown dot-dashed lines, respectively.

Pasalic and McGarry (2010), and details of the implementation shown in Appendix A. In general, the convolution terms can be discretized on either integer-grid or half-grid points, and the latter usually has better absorbing

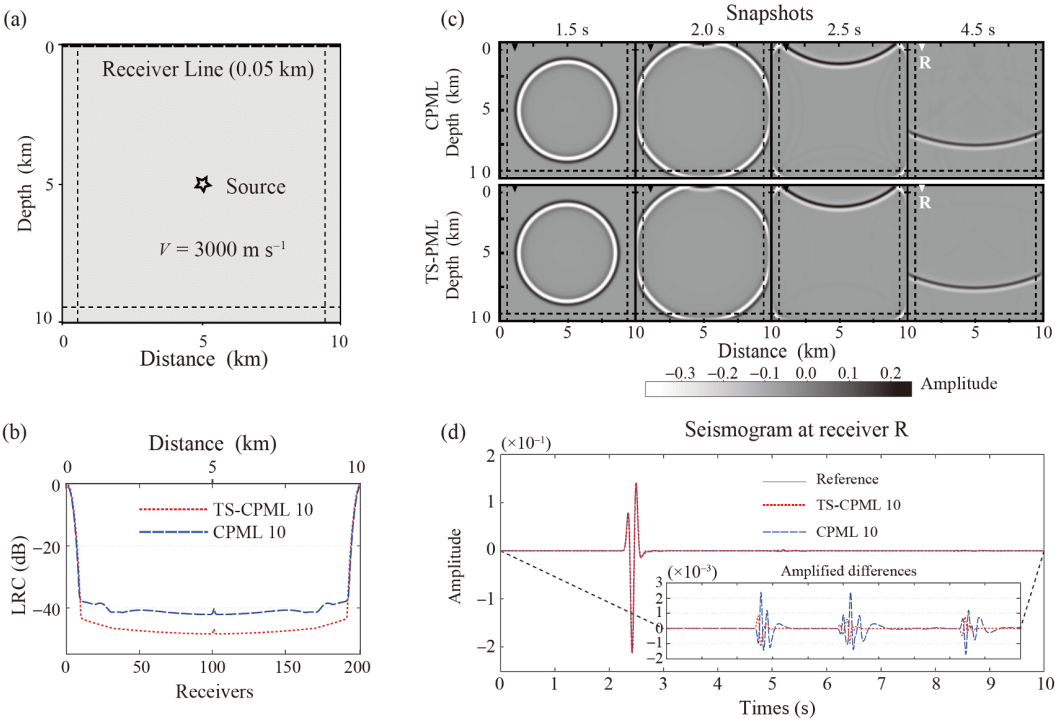

Figure 4 (a) The same 2-D homogeneous velocity model with a free surface on top. The thick horizontal dashed line indicates the locations of the 201 receivers. (b) LRCs measured at the 201 receivers based on the conventional CPML and the proposed TS-CPML are shown in blue dashed and red dotted lines, respectively. (c) Snapshots of the wavefields at 1.5, 2.0, 2.5 and 4.5 s from the conventional CPML and TS-CPML simulations are shown in the top and bottom lows, respectively. (d) Synthetic seismograms at the receiver R ($20\Delta x$, Δz) computed with CPML and TS-CPML are shown in blue dashed and red dotted lines, respectively. For comparison, the reference seismogram is also shown in a black solid line. Inset shows the enlarged differences between the two CPML synthetics and the reference trace.

performance. In our simulation, we discretized the convolution terms on integer grids. We also placed a point source at the center of the model (open star in Figure 4a) and computed LRCs along a horizontal line at the depth of 50 m (the thick black dashed line in Figure 4a). Figure 4b shows the calculated LRCs from the CPML (blue dashed line) and TS-CPML (red dotted line) using a 10-cell thick PML layer. In general, amplitudes of the reflections from the TS-CPML are two to three times smaller than those from the conventional CPML method. Note that the CPML results shown here are from the implementation of the second-order acoustic wave equation. Therefore, they are different from those shown in Figures 2 and 3, which are from simulations using the first-order wave equation.

In Figure 4c, we further show the wavefield snapshots of the CPML (top row) and TS-CPML simulations (bottom row) at four different times, 1.5, 2.0, 2.5, and 4.5 s. Indeed, reflections from the three PML boundaries are almost invisible in both simulations. In Figure 4d, we also plotted the synthetic seismograms at one of the receivers along the line, which is located at ($20\Delta x$, Δz) and indicated by a white reverse triangle in Figure 4c. The CPML and TS-CPML synthetics are shown in blue dashed and red dotted lines, respectively. We also show the reference synthetic seismogram (accurate solution) for comparison (Figure 4d). Again, the three traces are almost identical, manifesting the high absorbing efficiency in both implementations. We computed the differences between the PML synthetics and the reference trace, which are the computational errors of the two implementations. The enlarged differences shown in Figure 4d indicate that the CPML reflections from PML boundaries are ~1% of the direction arrival (blue dashed line in the inset of Figure 4d), while the TS-CPML reflections are less than 0.5%. Both the LRC and synthetics showed in Figure 4b and 4d demonstrated that our TS-CPML has a better absorbing performance than the conventional CPML implementation of the second-order wave equation.

Computationally, we also found that our TS-CPML technique has a slight advantage over the conventional CPML method. We employed a single CPU Linux machine with an intel e5-2680 v3 processor (12 cores) and a 128 GB memory card. The CPU time for a 2000-timestep simulation with the TS-CPML and CPML implementations is 0.67 and 0.72 s, respectively (Table 3). This is because the conventional CPML requires two more differential calculations at each grid point in the PML region than TS-CPML (Table 1 and Table 2).

3.2 Heterogeneous model

Next, to evaluate its performance in more complex velocity

Table 3 CPU times of the TS-CPML and CMPL

Method	Isotropic (2000 time-steps)	TTI acoustic (10000 timesteps)
TS-CPML (s)	0.67	485
CPML (s)	0.72	493

models, we applied the TS-CPML scheme to the 2D SEG/EAGE salt model with a free-surface boundary on top. The model is shown in Figure 5. The total size of the model is 32.45 km×7.5 km consisting of a computational domain of 629Δx×140Δz in the middle surrounded by a 10-cell thick PML layer in the left side, right side, and the bottom. We placed a Ricker wavelet source at (15 km, 1.0 km), which had a dominant frequency f_0=5 Hz and a shifted time t_0=0.3 s.

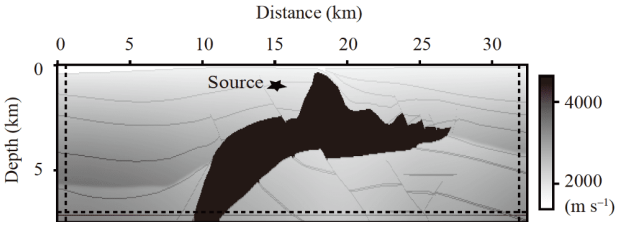

Figure 5 The 2-D SEG/EAGE salt velocity model. It has a free-surface boundary on top and has a dimension of 32.45 km×7.5 km, which was discretized into 649 cells in x direction and 150 cells in z direction.

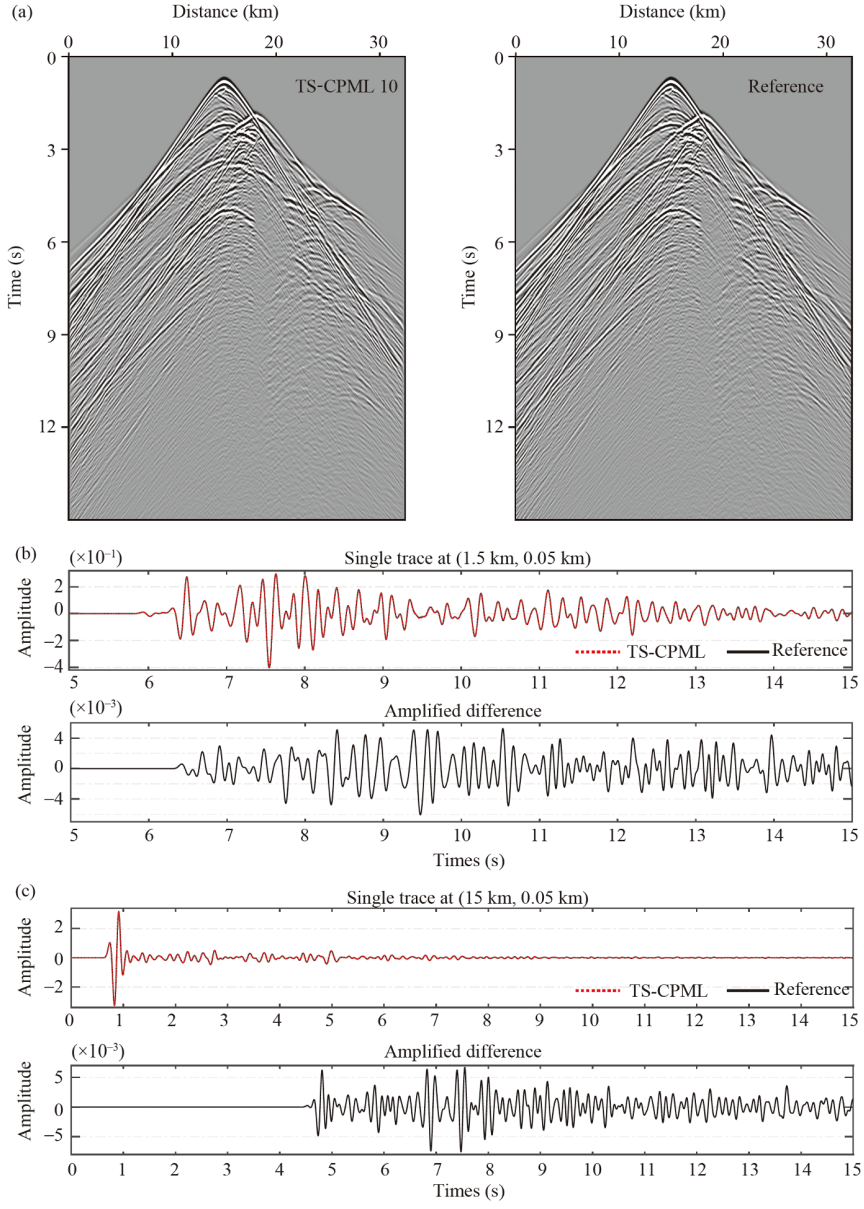

Figure 6 Comparison of TS-CPML synthetics computed from the 2-D SEG/EAGE model shown in Figure 5 with a 10-cell thick PML layer and reference traces. (a) The left panel shows the TS-CPML synthetics recorded at a linear array deployed along the second row of the model grids at a depth Δz=0.05 km, while the right panel is the reference record section. Note the high similarity between the two panels. (b) The top row shows the TS-CPML synthetic seismogram and the reference trace at (30Δx, Δz), and the bottom row shows the enlarged differences between them. (c) Same as shown in (b) except for a different location (300Δx, Δz).

Figure 6a shows the TS-CPML synthetic seismograms recorded by hypothetic sensors located along a horizontal line at the depth of 50 m in the left panel, and the reference traces in the right for comparison. The two record sections look almost the same and the TS-CPML records show no clear artificial reflections and low-frequency noise. To quantify the absorbing performance of TS-CPML, we selected two seismic traces recorded at x=1.5 km and x=15 km at the same depth (50 m), which are plotted in Figure 6b and 6c, respectively. In each location, the TS-CPML synthetic matches almost perfectly with the reference trace. The enlarged differences between the TS-CPML and reference synthetics suggest that the TS-CPML technique can achieve high accuracy in a strong heterogeneous model using a thin PML layer of only 10-cell thick.

3.3 Anisotropic model

We further verified the performance of TS-CPML and analyzed the absorbing and computational efficiency between the conventional CPML (Appendix B for more details) and TS-CPML in an anisotropic velocity model. Figure 7 shows the TTI model used in our simulation. It is part of the 2D BP TTI model with a free-surface boundary on top. The total size of the model is 4.5 km×4.5 km, surrounding a computational domain with a PML layer of 30-cell thick on both sides and the bottom. We applied the TS-CPML scheme to the second-order pseudo-acoustic TTI wave equation (eq. (20)). We employed a Ricker wavelet source with a dominant frequency f_0=25 Hz, which was placed at (500Δx, 5Δz). We employed a grid spacing of Δx=Δz=5 m and time step of Δt=5 ms in this FD simulation.

Figure 8a shows the TS-CPML (left) and CPML (middle) synthetics computed at the grids at Δz=5 m below surface, respectively. We also show the reference record section (right) for comparison. The three record sections appear to be very similar, suggesting that there are no obvious reflections from the model boundaries (two sides+bottom). We further plotted the synthetic seismograms computed by the TS-CPML and CPML methods at (0.25 km, 0.005 km) in Figures 8b. Their differences with respect to the reference trace are shown in Figure 8c. The computational errors (Figure 8c) indicate that artificial reflections on the conventional CPML seismogram are approximately two times as large as those on the TS-CPML synthetic data, suggesting that the TS-CPML scheme has better absorbing performance for wavefield simulations in TTI media as well. As far as for the CPU times, we employed the same processor mentioned in Section 3.1, and ran the simulations for a total of 10000 timesteps (i.e., a total of 5 s). The total simulation time is 485 s for the TS-CPML and 493 s for the conventional CPML methods (Table 3). Table 2 also lists all the convolution terms and first-order spatial derivatives involved in the two implementations of wavefield simulations in TTI media.

We further extended the simulation to 70000 timesteps and obtained a total of 35s of the wavefield. For each timestep, we computed the total energy of the wavefield by summing energy at each grid point in both the computational and PML

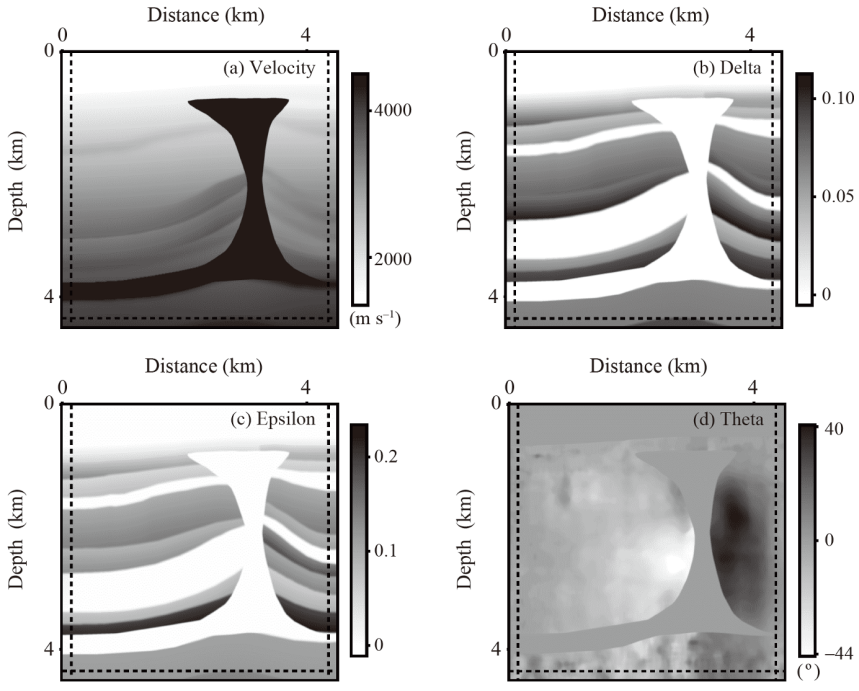

Figure 7 The anisotropic model is taken from a portion of the 2-D BP TTI model with a free-surface boundary on top. The model has a dimension of 4.5 km×4.5 km, consisting of 900 cells in x direction and 900 cells in z direction. The thin dashed lines separate the computational and the PML domains. The isotropic velocity and the three Thomsen anisotropic parameters are showing in (a)–(d), respectively.

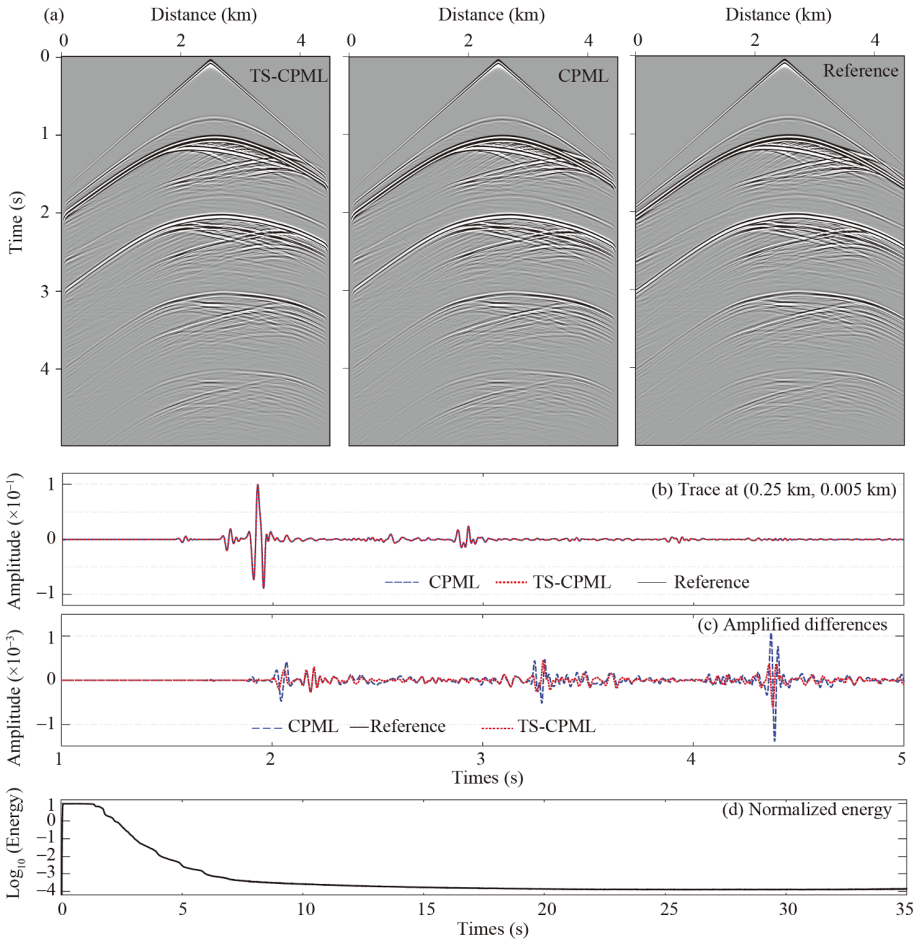

Figure 8 Comparison of TS-CPML synthetics, conventional CPML synthetics and reference traces computed with the 2-D BP TTI model shown in Figure 7. (a) These sections comprise 901 seismograms recorded at a depth of Δz=5 m from the free surface. Note the high similarity between the three sections. (b) The conventional CPML (blue dashed line) and TS-CPML synthetics (red dotted line) are shown together with the accurate solution (black solid line) at location (0.25 km, 0.005 km) for comparison. (c) The enlarged differences between the CPML and TS-CPML synthetics and the reference trace. Note the CPML seismogram shows larger artificial reflections than the TS-CPML simulation does. (d) Normalized total energy integrated from the computational and CPML domains is shown as a function of wavefield propagation time, which was simulated up to 35 s (70000 timesteps).

domains. We found that the total energy is stable at the beginning of the simulation, starts to decay once waves enter to the PML regions (Figure 8d), suggesting that TS-CPML is a stable implementation in the TTI medium during the 35 s numerical simulation test.

4. Conclusions

We propose a new TS-CPML scheme for numerical modeling of the acoustic wavefield. This allows one to use the unsplit complex frequency shifted PML boundary condition based on the recursive convolution technique. Our new TS-CPML approach can be applied to both isotropic and anisotropic second-order acoustic wave equations directly and efficiently. The TS-CPML is relatively easy to implement, and numerical simulations have demonstrated its excellent performance in absorbing boundary reflections. Our numerical tests have also shown that the TS-CPML method has better absorbing and computational efficiency than the conventional CPML implementation to the second-order wave equations.

Acknowledgements *We thank Drs. Yang ZHAO and Gang YAO at the China University of Petroleum at Beijing for helpful discussion. We also thank the associate editor and two anonymous reviewers for their constructive and thoughtful comments and suggestions, which have significantly improved the quality of this paper. This work was supported by the National Natural Science Foundation of China (Grant No. 41630209).*

References

Alford R, Kelly K, Boore D M. 1974. Accuracy of finite-difference modeling of the acoustic wave equation. Geophysics, 39: 834–842

Appelö D, Kreiss G. 2007. Application of a perfectly matched layer to the nonlinear wave equation. Wave Motion, 44: 531–548

Bérenger J P. 1994. A perfectly matched layer for the absorption of electromagnetic waves. J Comput Phys, 114: 185–200

Bérenger J P. 2002a. Application of the CFS PML to the absorption of evanescent waves in waveguides. IEEE Microw Wireless Compon Lett, 12: 218–220

Bérenger J P. 2002b. Numerical reflection from FDTD-PMLs: A comparison of the split PML with the unsplit and CFS PMLs. IEEE Trans

Antennas Propagat, 50: 258–265
Basu U, Chopra A K. 2004. Perfectly matched layers for transient elastodynamics of unbounded domains. Int J Numer Meth Eng, 59: 1039–1074
Becache E, Petropoulos P G, Gedney S D. 2004. On the long-time behavior of unsplit perfectly matched layers. IEEE Trans Antennas Propagat, 52: 1335–1342
Chen H, Zhou H, Li Y. 2014. Application of unsplit convolutional perfectly matched layer for scalar arbitrarily wide-angle wave equation. Geophysics, 79: T313–T321
Chew W, Liu Q. 1996. Perfectly matched layers for elastodynamics: A new absorbing boundary condition. J Comput Acoust, 4: 341–359
Collino F, Tsogka C. 2001. Application of the perfectly matched absorbing layer model to the linear elastodynamic problem in anisotropic heterogeneous media. Geophysics, 66: 294–307
Duru K, Kreiss G. 2012. A well-posed and discretely stable perfectly matched layer for elastic wave equations in second order formulation. Commun Comput Phys, 11: 1643–1672
Drossaert F H, Giannopoulos A. 2007a. A nonsplit complex frequency-shifted PML based on recursive integration for FDTD modeling of elastic waves. Geophysics, 72: T9–T17
Drossaert F H, Giannopoulos A. 2007b. Complex frequency shifted convolution PML for FDTD modelling of elastic waves. Wave Motion, 44: 593–604
Festa G, Nielsen S. 2003. PML absorbing boundaries. Bull Seismol Soc Am, 93: 891–903
Festa G, Vilotte J P. 2005. The newmark scheme as velocity-stress time-staggering: An efficient PML implementation for spectral element simulations of elastodynamics. Geophys J Int, 161: 789–812
Festa G, Delavaud E, Vilotte J P. 2005. Interaction between surface waves and absorbing boundaries for wave propagation in geological basins: 2D numerical simulations. Geophys Res Lett, 32: L20306
Fletcher R P, Du X, Fowler P J. 2009. Reverse time migration in tilted transversely isotropic (TTI) media. Geophysics, 74: WCA179–WCA187
Gao Y, Zhang J, Yao Z. 2015. Unsplit complex frequency shifted perfectly matched layer for second-order wave equation using auxiliary differential equations. J Acoust Soc Am, 138: EL551–EL557
Graves R W. 1996. Simulating seismic wave propagation in 3D elastic media using staggered-grid finite differences. Bull Seismol Soc Amer, 86: 1091–1106
Hastings F D, Schneider J B, Broschat S L. 1996. Application of the perfectly matched layer (PML) absorbing boundary condition to elastic wave propagation. J Acoust Soc Am, 100: 3061–3069
Kelly K, Ward R, Treitel S, Alford R. 1976. Synthetic seismograms: A finite-difference approach. Geophysics, 41: 2–27
Kindelan M, Kamel A, Sguazzero P. 1990. On the construction and efficiency of staggered numerical differentiators for the wave equation. Geophysics, 55: 107–110
Kuzuoglu M, Mittra R. 1996. Frequency dependence of the constitutive parameters of causal perfectly matched anisotropic absorbers. IEEE Microw Guid Wave Lett, 6: 447–449
Komatitsch D, Martin R. 2007. An unsplit convolutional perfectly matched layer improved at grazing incidence for the seismic wave equation. Geophysics, 72: SM155–SM167
Kreiss G, Duru K. 2013. Discrete stability of perfectly matched layers for anisotropic wave equations in first and second order formulation. Bit Numer Math, 53: 641–663
Levander A R. 1988. Fourth-order finite-difference *P-SV* seismograms. Geophysics, 53: 1425–1436
Li Y, Matar O B. 2010. Convolutional perfectly matched layer for elastic second-order wave equation. J Acoust Soc Am, 127: 1318–1327
Li S Z, Sun C Y, Tian L, Peng P P, Qiu Y. 2018. Unsplit complex frequency shifted PML implementation in mess-free discretization. In: 80th Annual International Conference and Exhibition, EAGE, Extended Abstracts
Liu Y, Sen M K. 2009. A new time–space domain high-order finite-difference method for the acoustic wave equation. J Comput Phys, 228: 8779–8806
Liu Y. 2014. Optimal staggered-grid finite-difference schemes based on least-squares for wave equation modelling. Geophys J Int, 197: 1033–1047
Marcinkovich C, Olsen K. 2003. On the implementation of perfectly matched layers in a three-dimensional fourth-order velocity-stress finite difference scheme. J Geophys Res, 108: 2276–2292
Marfurt K J. 1984. Accuracy of finite-difference and finite-element modeling of the scalar and elastic wave equations. Geophysics, 49: 533–549
Martin R, Komatitsch D, Ezziani A. 2008. An unsplit convolutional perfectly matched layer improved at grazing incidence for seismic wave propagation in poroelastic media. Geophysics, 73: T51–T61
Martin R, Komatitsch D. 2009. An unsplit convolutional perfectly matched layer technique improved at grazing incidence for the viscoelastic wave equation. Geophys J Int, 179: 333–344
Martin R, Komatitsch D, Gedney S D, Bruthiaux E. 2010. A high-order time and space formulation of the unsplit perfectly matched layer for the seismic wave equation using auxiliary differential equations (ADE-PML). Comput Model Eng Sci, 56: 17–42
Ma X, Yang D, Huang X, Zhou Y. 2018. Nonsplit complex-frequency shifted perfectly matched layer combined with symplectic methods for solving second-order seismic wave equations—Part 1: Method. Geophysics, 83: T301–T311
Ma X, Yang D, He X, Huang X, Song J. 2019a. Nonsplit complex-frequency-shifted perfectly matched layer combined with symplectic methods for solving second-order seismic wave equations—Part 2: Wavefield simulations. Geophysics, 84: T167–T179
Ma X, Li Y, Song J. 2019b. A stable auxiliary differential equation perfectly matched layer condition combined with low-dispersive symplectic methods for solving second-order elastic wave equations. Geophysics, 84: T193–T206
Pasalic D, McGarry R. 2010. Convolutional perfectly matched layer for isotropic and anisotropic acoustic wave equations. In: 80th Annual International Meeting. SEG, Expanded Abstracts. 2925–2929
Ramadan O. 2003. Auxiliary differential equation formulation: An efficient implementation of the perfectly matched layer. IEEE Microw Wireless Compon Lett, 13: 69–71
Roden J A, Gedney S D. 2000. Convolution PML (CPML): An efficient FDTD implementation of the CFS-PML for arbitrary media. Microw Opt Technol Lett, 27: 334–339
Saenger E H, Gold N, Shapiro S A. 2000. Modeling the propagation of elastic waves using a modified finite-difference grid. Wave Motion, 31: 77–92
Thomsen L. 1986. Weak elastic anisotropy. Geophysics, 51: 1954–1966
Virieux J. 1984. *SH*-wave propagation in heterogeneous media: Velocity-stress finite-difference method. Geophysics, 49: 1933–1942
Virieux J. 1986. *P-SV* wave propagation in heterogeneous media: Velocity-stress finite-difference method. Geophysics, 51: 889–901
Wang T, Tang X. 2003. Finite-difference modeling of elastic wave propagation: A nonsplitting perfectly matched layer approach. Geophysics, 68: 1749–1755
Wang Y, Liang W, Nashed Z, Li X, Liang G, Yang C. 2014. Seismic modeling by optimizing regularized staggered-grid finite-difference operators using a time-space-domain dispersion-relationship-preserving method. Geophysics, 79: T277–T285
Zhang W, Shen Y. 2010. Unsplit complex frequency-shifted PML implementation using auxiliary differential equations for seismic wave modeling. Geophysics, 75: T141–T154
Zhang Z, Zhang W, Chen X. 2014. Complex frequency-shifted multi-axial perfectly matched layer for elastic wave modelling on curvilinear grids. Geophys J Int, 198: 140–153

(Responsible editor: Dinghui YANG)